Karlsruher Institut für Technologie

Defects at Silica Surfaces and crack-tip shielding-

A Finite Element Study

Open Access at KIT

Gabriele Rizzi, Theo Fett

KIT SCIENTIFIC WORKING PAPERS 33

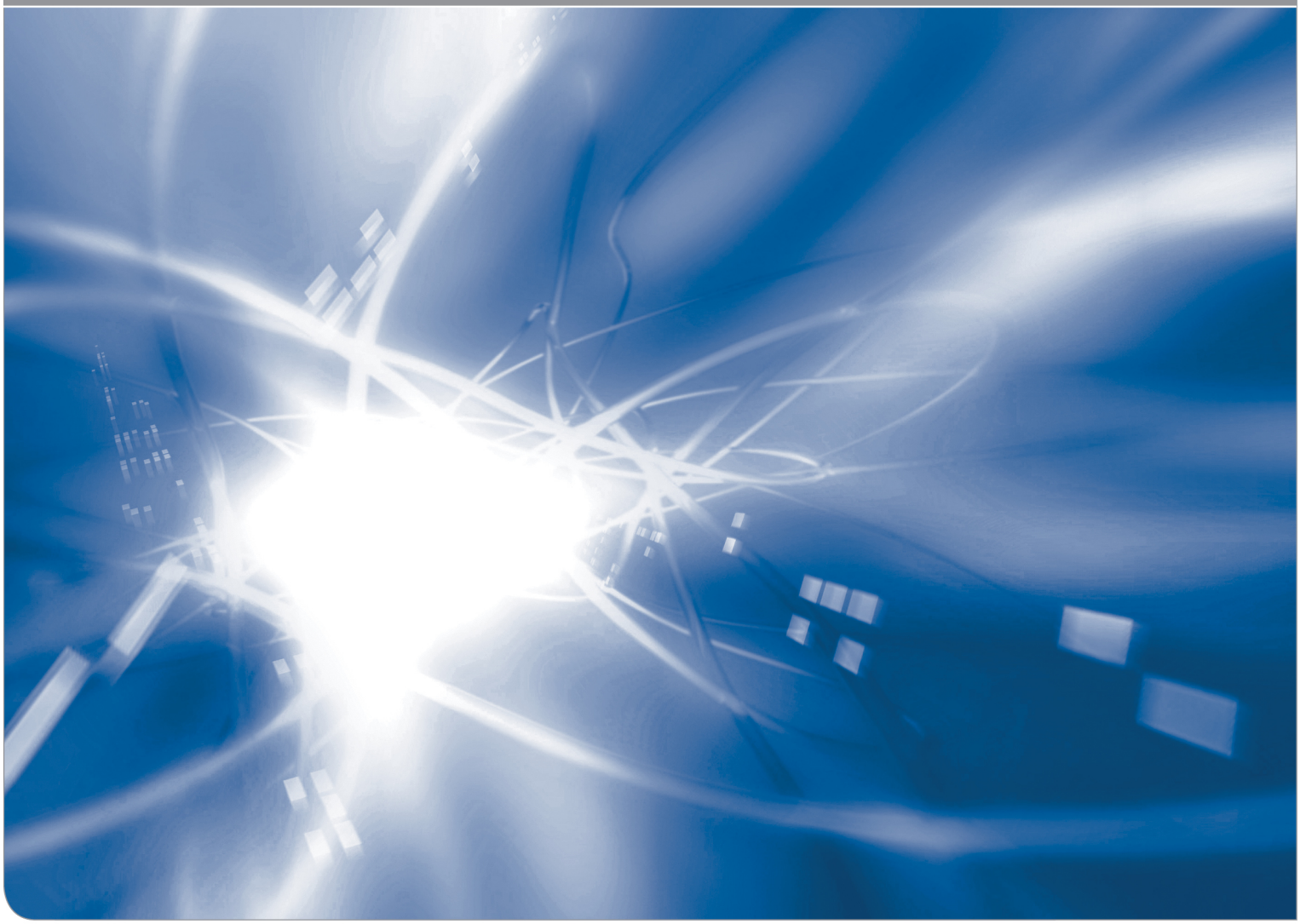

KIT – Universität des Landes Baden-Württemberg und nationales Forschungszentrum in der Helmholtz-Gemeinschaft

Institut für Angewandte Materialien, Karlsruher Institut für Technologie (KIT)

Impressum

Karlsruher Institut für Technologie (KIT)
www.kit.edu

2015

ISSN: 2194-1629
DOI: 10.5445/IR/1000049272

Abstract

The prediction of strength in silica needs knowledge of failure behaviour of defects in the surface region. Two types of defects are studied by using the Finite Element method:

1. Due to the SiO_2 ring structure there exist pore-like regions in the material with diameter in the order of nanometers. They may be modeled by spherical pores. At the surface we assume half-spheres.

2. Surface corrosion in humid environments may result in a high density of surface defects, which can interact. Such defects are treated by assuming sharp cracks.

3. Crack-like surface defects undergo swelling when they are exposed to mechanical stresses. This must affect strength behaviour.

The results for pores are given in terms of stresses, the results for cracks by stress intensity factors.

Contents

A) CRACKS

A) PORES

A) CRACKS

1. Single edge crack

The water penetrated through the surface reacts with the silica network according to [1]

$$\equiv\text{Si-O-Si}\equiv + H_2O \leftrightarrow \equiv\text{SiOH}+\text{HOSi}\equiv \quad (1)$$

with the concentration of the hydroxyl $S = [\equiv\text{SiOH}]$ and that of the molecular water $C = [H_2O]$. In the following considerations it is assumed for clearness that the equilibrium of (2) is already reached.

A single crack embedded in a swelling zone of height ω and constant volume swelling is shown in Fig. 1. The crack length, a, and the zone height are negligibly small compared to the specimen dimensions.
Zones of different heights were modelled in a finite element (FE) study. The case of a half-space was realized by a plate of width 50ω and height 100ω. Solid continuum elements (8-node bi-quadratic) were chosen and the computations carried out with ABAQUS Version 6.8. The volume strain was replaced by the equivalent thermal problem by heating the swelling zone by ΔT keeping T=0 in the rest of the structure.
This results in the strain

$$\varepsilon_v = 3\alpha\Delta T \quad (2)$$

(α=thermal expansion coefficient).

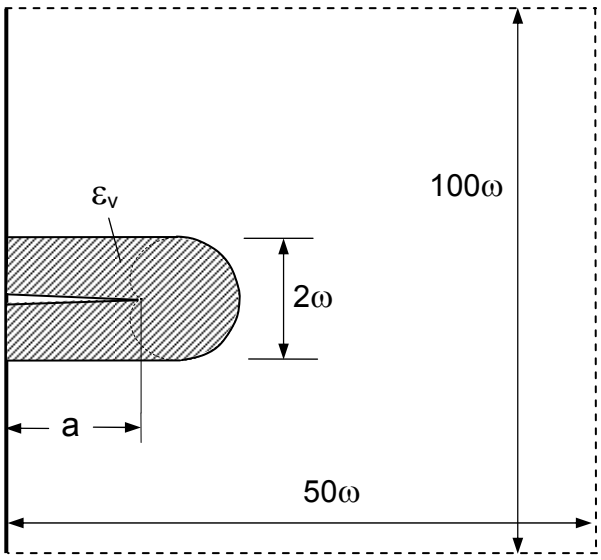

Fig. 1 Single edge crack in a semi-infinite specimen embedded in a swelling zone.

The shielding stress intensity factors from FE-computations normalized on the value $K_{sh}(0)$, i.e. for the semi-infinite crack with ω/a=0 [2], are plotted in Fig. 2 as a function of the ratio of ω/a.

The FE-results given by the circles can be expressed by the relation

$$K_{sh}(\omega/a) \cong K_{sh}(0)\exp\left[-1.18\frac{\omega}{a}\right] \tag{3}$$

with

$$K_{sh}(0) = -\psi(0)\frac{\varepsilon_v E}{1-\nu}\sqrt{\omega} \tag{4}$$

and different zone shape

$$\psi(0) = \begin{cases} 0.22 & \text{for heart shape} \\ 0.25 & \text{for semi circle} \end{cases} \tag{5}$$

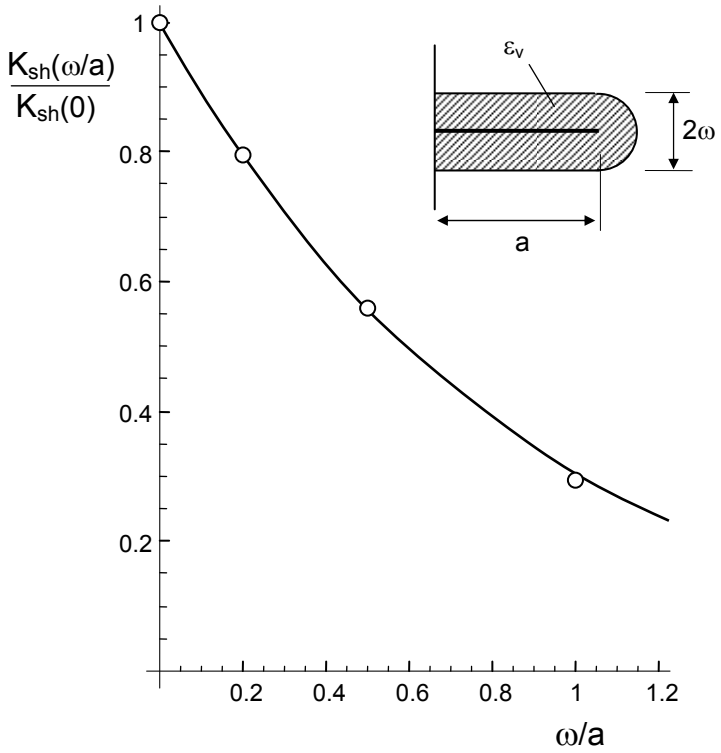

Fig. 2 Shielding stress intensity factor as a function of the relative zone height.

From the solution in Fig. 2 the shielding stress intensity factor for any swelling distribution can be determined using the Green's function as outlined in [3]. The shielding contribution of a zone of thickness dω' at the height coordinate ω' (Fig. 3) is

$$dK_{sh} = -\psi\frac{\varepsilon_v E}{(1-\nu)\sqrt{\omega'}}1.18\exp\left[-1.18\frac{\omega'}{a}\right]\left(0.4237-\frac{\omega'}{a}\right)d\omega' \tag{6}$$

defining the Green's function

$$h(\omega') = -\psi\frac{\varepsilon_v E}{(1-\nu)\sqrt{\omega'}}1.18\exp\left[-1.18\frac{\omega'}{a}\right]\left(0.4237-\frac{\omega'}{a}\right)' \tag{7}$$

This function allows to determine the shielding stress intensity factor for an arbitrarily given strain distribution ε(ω')

$$K_{sh} = \int_0^{\infty} \varepsilon(\omega')\, h(\omega')\, d\omega' \tag{8}$$

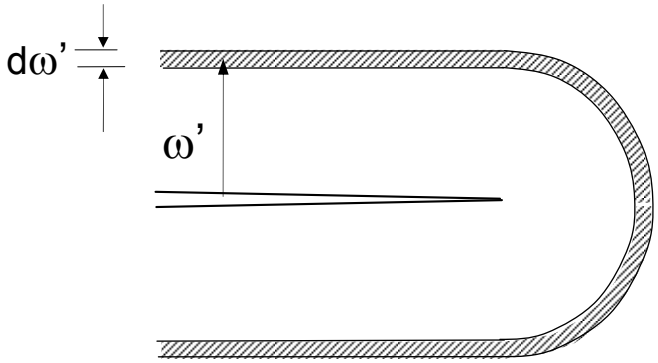

Fig. 3 Shape of a differential layer of thickness dω' in a zone with constant hydroxyl concentration.

2. Multiple edge cracks

2.1 Applied stress intensity factor

Figure 4 shows an array of identical edge cracks. The applied stress intensity factors are known from literature [4].

We can represent these data by the simple relation [5]

$$K_{appl} = \sigma_{appl} \sqrt{c/2}\, \tanh^{5/11}\left(1.122\sqrt{2\pi}\sqrt{\frac{a}{c}}\right)^{11/5} \tag{9}$$

with the *constant* solution for long cracks, $a > c/3$

$$K_{appl} = \sigma_{appl} \sqrt{c/2} \tag{10}$$

independent on the crack depth a. This fact is very important. Equation (9) is plotted in Fig. 4b. For half-penny shaped surface cracks the solution deviates for $a/c > 0.5$ less than 10% as can be seen from Isida and Tsuru [6]. In the following computations we therefore consider the surface cracks as edge cracks.

Whereas the single-crack solution increases continuously with increasing crack length, the stress intensity factor for the crack array remains constant for larger than $a/c \approx 1/3$.

2.2 Shielding stress intensity factor

Swelling behaviour of multiple cracks is the same as for a single crack. This is illustrated in Fig. 5a for a subcritically grown crack with heart-shaped zone front contour and in Fig. 5b for an unloaded crack array showing semi-circular zone fronts. The crack array with the semi-circular zone front contour and the same swelling zone of height ω for each crack yields the shielding stress intensity factors of Fig. 5.

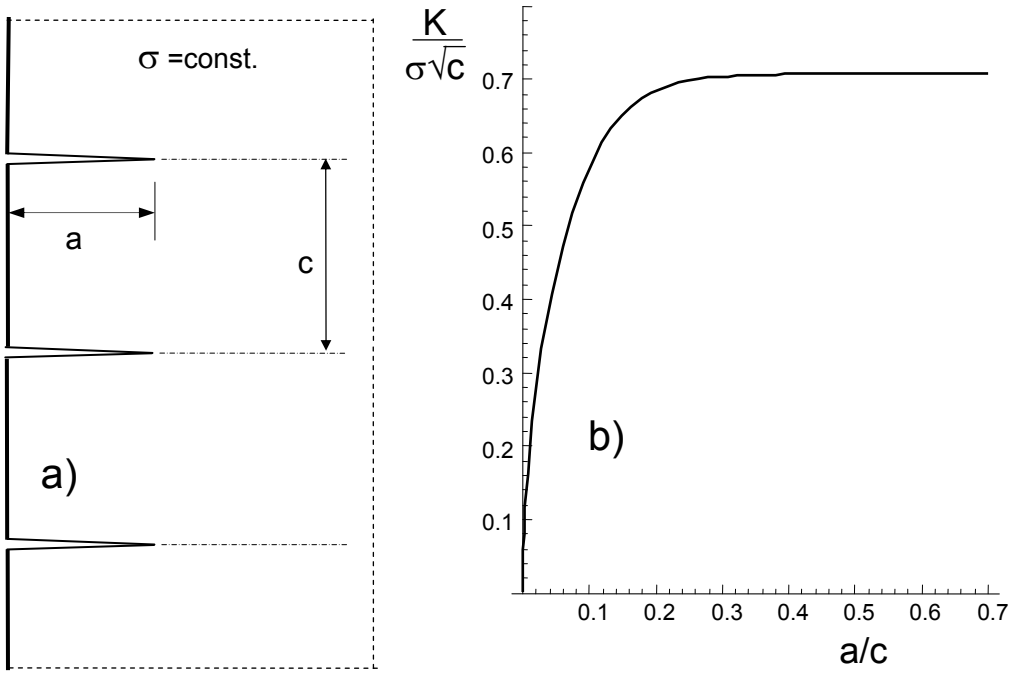

Fig. 4 a) Array of edge cracks under remote load σ, b) stress intensity factor solution.

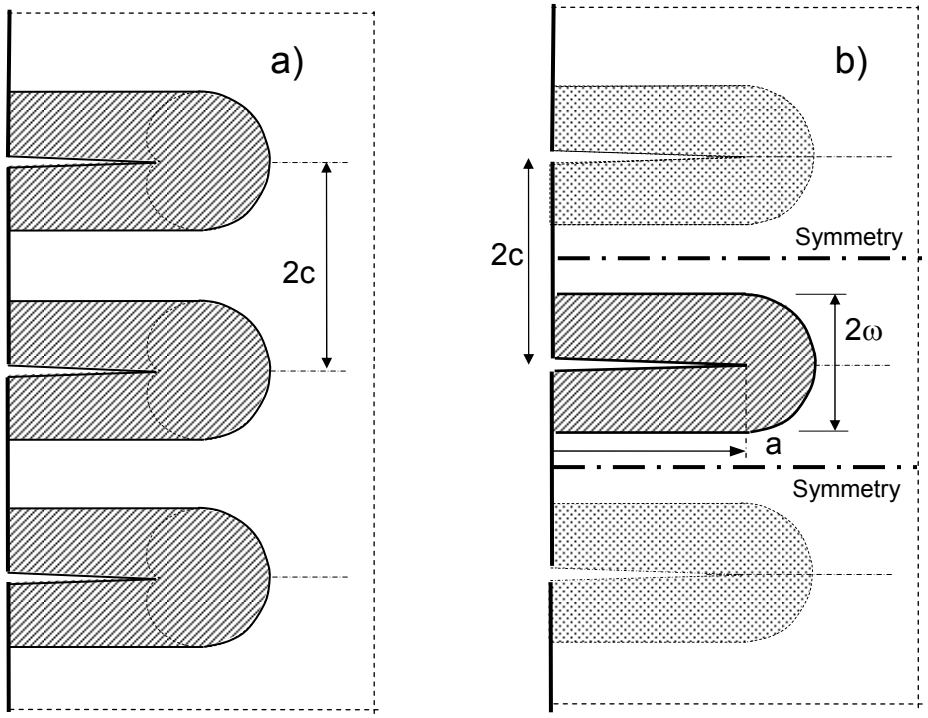

Fig. 5 a) Swelling zones of growing multiple cracks, b) modelling by a single crack introducing symmetry planes.

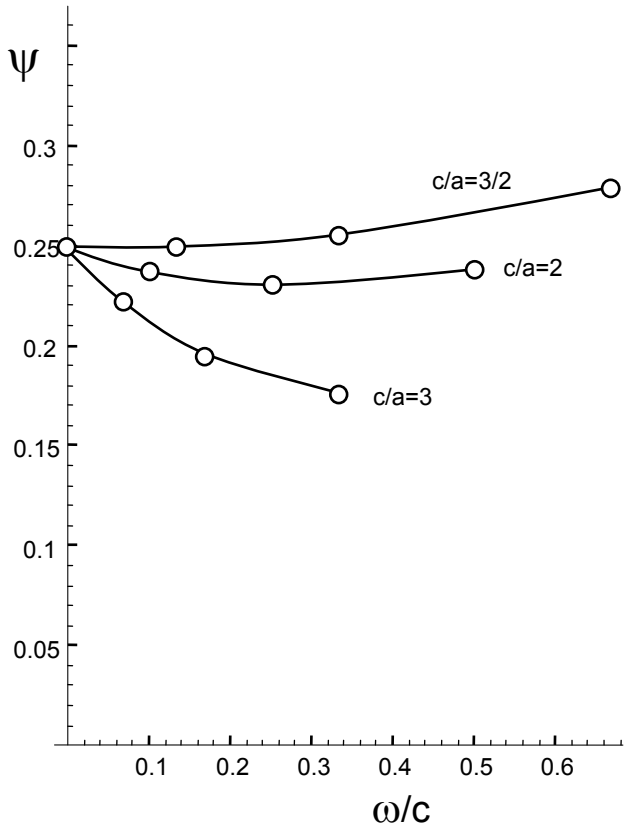

Fig. 6 Shielding stress intensity factors for multiple cracks (semi-circular zone ends).

3. Stress-enhanced swelling zones at short surface cracks

In the case of a *long crack* of length a with a swelling zone height ω small compared to the crack length, $\omega << a$, the heart-shaped zone for an arrested crack yields a disappearing shielding stress intensity factor $K_{sh}=0$ [7]. The height of the contour for the hydrostatic stress is in this case

$$\omega = \frac{(1+\nu)^2}{4\sqrt{3}\pi}\left(\frac{K_I}{\sigma_h}\right)^2 \tag{11}$$

For the computation of the swelling zones ahead of very *short surface cracks*, $\omega \approx a$, a Finite Element analysis was performed. Figure 7 shows such a crack together with contours for constant hydrostatic stresses σ_h, which under "weak swelling" conditions describe the shape of the swelling zones (dashed contours). This treatment is similar to the case of "weak phase transformation" assuming that the stress field caused by a phase transformation in zirconia ceramics does not affect the stress field triggering the transformation [7,8]. The solid contours in Fig. 7 show the contours of hydrostatic stresses σ_h for a tensile stress σ_{appl}. For a crack of depth a, the stress intensity factor results as

$$K = 1.122\sigma_{appl}\sqrt{\pi a} \tag{12}$$

which is used in Fig. 8 for scaling the ordinate.

In Fig. 8 the zone heights from FE are compared with the near-tip stresses as resulting from the long-crack solution

$$\sigma_h = \tfrac{2}{3}(1+\nu)\frac{K}{\sqrt{2\pi r}}\cos(\varphi/2)\,, \quad r = \frac{\omega}{\sin \pi/3} \tag{13}$$

For $\omega/a \leq 1/4$, differences are negligible.

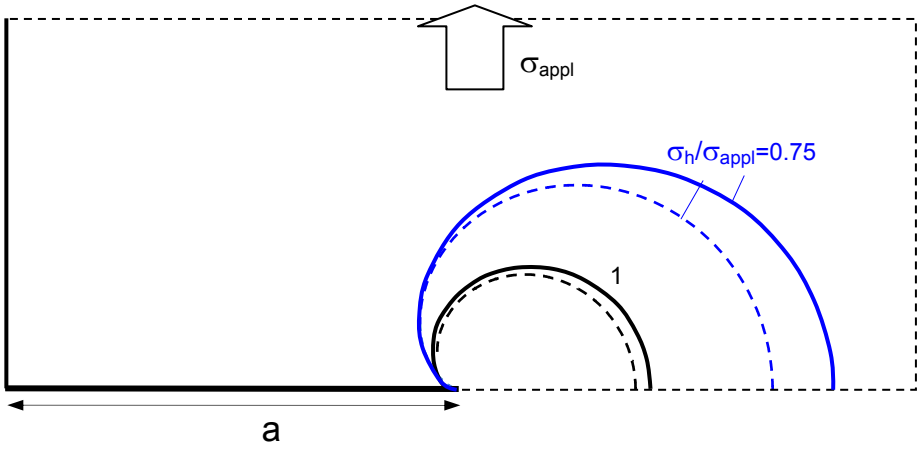

Fig. 7 Contours of hydrostatic stress field ahead of a short crack with depth a in a semi-infinite plate loaded by a tensile stress σ_{appl} (solid curves). The dashed contours show the related long-crack solution with $\omega/a \to 0$.

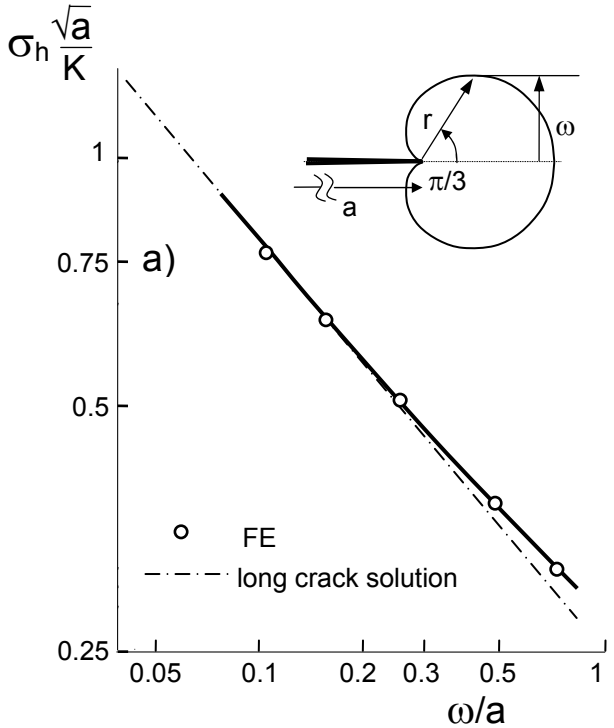

Fig. 8 Hydrostatic stress at a crack under tension, comparison of short-crack results obtained via FE with the solution for a long crack according to McMeeking and Evans [7]; (contour for constant hydrostatic stress as insert).

4. A crack passing the initial swelling zone

During the soaking treatment under tension the crack-tip region is surrounded by a swelling zone. The shielding stress intensity factor caused by this zone is given by [7]

$$K_{sh,2} = -\psi \frac{\varepsilon_v E}{1-\nu}\sqrt{\omega} \tag{14}$$

When crack propagation has taken place during soaking, the swelling zone extends with crack length as illustrated in Fig. 9b. For the case of weak swelling as discussed by McMeeking and Evans [7] the heart-shaped contour remains ahead of the tip and the coefficient is ψ=0.22.

After high-temperature soaking, these swelling zones are maintained at room temperature where the strength tests are performed.

When the crack undergoes continuously increasing loading, the crack must extend and will escape of the initial swelling zone. Concequently, the coeffient ψ in eq.(14) must become dependent on the crack extension Δa in the strength test. The red curve in Fig. 9c represents analytical results for a heart-shaped swelling zone we got by application of the McMeeking and Evans [7] procedure. A maximum of ψ is reached at $\Delta a/\omega = 8/\sqrt{27} \cong 1.54$ with $\psi \approx 0.3$. In the case of a grown crack with extended swelling zone (black curve) it results $\psi \approx 0.33$.

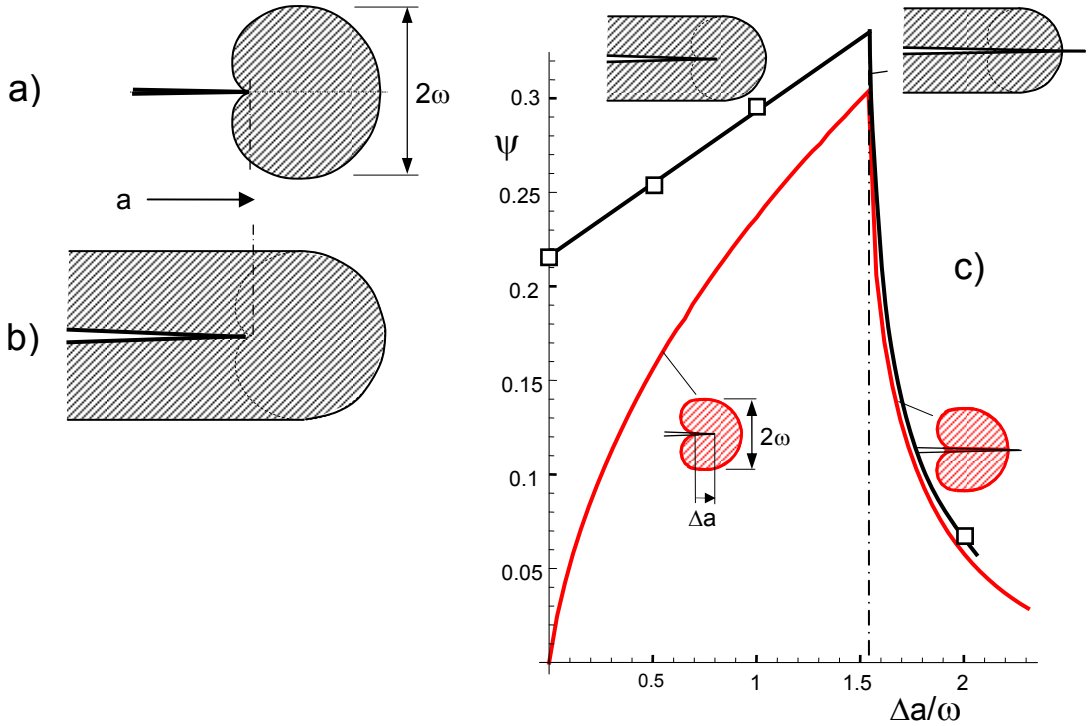

Fig. 9 a) Swelling zone for an arrested crack, b) grown crack for weak swelling, c) shielding stress intensity factor for crack extension through the initially swelling zone, red curve: crack passing the initial zone developing for an arrested crack, obtained by application of the procedure by McMeeking and Evans [7]; black: grown crack after additional extension Δa obtained from FE-analysis.

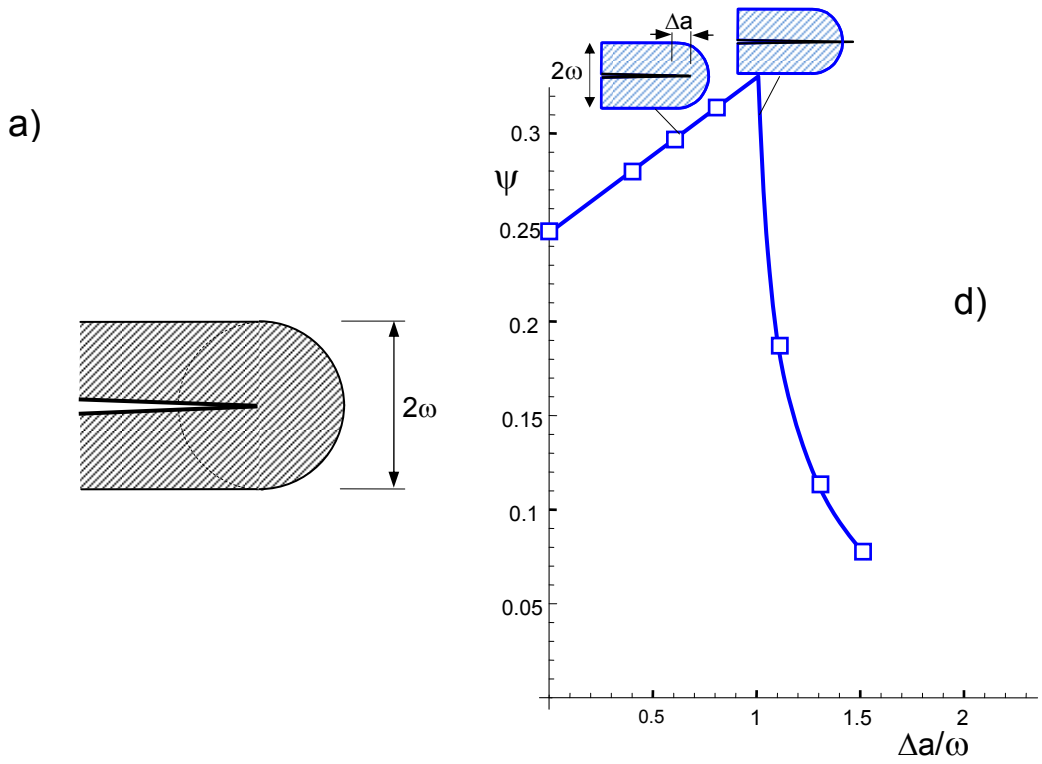

Fig. 10 FE-results for a for a circular zone shape from [9].

5. Crack opening displacements

5.1 Crack opening in zones with reduced Young's module

The crack opening displacement δ for a crack in a homogeneous material with Young's modulus E under an externally applied load is given by the so-called Irwin parabola. When K_{appl} denotes the related stress intensity factor, it holds for plane stress conditions as present in very thin test specimens

$$\delta = \sqrt{\frac{8}{\pi}} \frac{K}{E} \sqrt{r} + O(r) \tag{15}$$

When a hydroxyl has been formed, the initial silica ring is broken and the mechanical cohesion is weakened. The consequence is a reduction in the Young's modulus, E. The stress-enhanced reaction (1) results in heart-shaped damage zones for the case that swelling stresses are neglected ("weak swelling"), shaded region in Fig. 11. This result is identical to the case of "weak phase transformation" assuming that the stress field caused by a phase transformation in zirconia ceramics does not affect the stress field triggering the transformation [7,8].

When swelling contributes considerably to the stresses ("strong swelling"), the zone shape changes. The influence of "strong swelling" on the shape of the swelling zones was studied in [10, 11] with the result that the zone shape tends against a circular contour as indicated by the dashed curve in Fig. 11.

5.2 Computation of crack opening displacements (COD) for an arrested crack

In the case of the crack tip located in the damage zone (dashed curve in Fig. 11), the near-tip displacements can be computed analytically.

In a material with varying Young's modulus, the fracture mechanics J-Integral as the driving force for crack extension remains path-independent, i.e. any path in the near-tip region, J_{tip}, must give the same result as a path far away from the crack, J_∞. In the case of linear-elastic fracture mechanics, the J-integral is identical with the energy release rate G. If E and ν stand for the Young's modulus and Poisson ratio at the tip and E_0 and ν_0 for the bulk material, it results

$$\frac{K_{tip}^2}{E}(1-\nu^2) = \frac{K_{appl}^2}{E_0}(1-\nu_0^2) \tag{16}$$

In (16) K_{tip} is the "true" stress intensity factor acting at the tip and K_{appl} is the externally applied stress intensity factor that can be computed from handbook solutions. Under plane stress conditions, we get from (16)

$$K_{tip} = K_{appl}\sqrt{\frac{E}{E_0}} \tag{17}$$

Introducing this result into eq.(15) yields finally

$$\delta = \sqrt{\frac{8}{\pi}}\frac{K_{appl}}{E_0}\sqrt{\frac{E_0}{E}}\sqrt{r} + O(r) \tag{18}$$

For the heart-shaped zone (hatched area in Fig. 11), the displacement behaviour is much more complicated. In this case, the crack tip belongs as well to the zone of low modulus E as to the outer region with Young's module E_0.

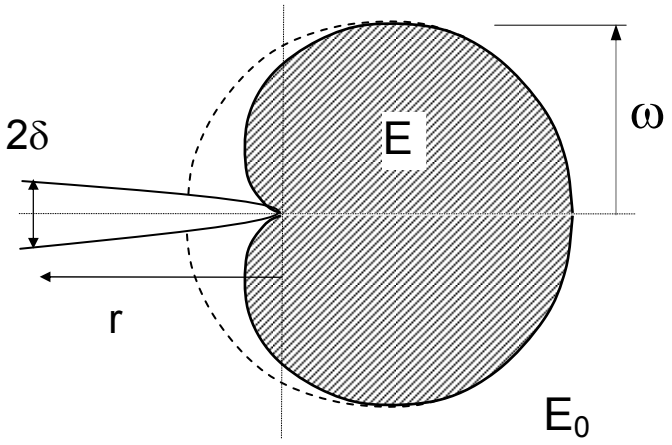

Fig. 11 Crack-tip region under load showing damage zones for "weak swelling" conditions (hatched heart-shaped area) and "strong swelling" (dashed curve).

We studied the displacements in a FE-study on heart-shaped zones of height ω in a plate of width=60ω and height=60ω showing constant Young's module, E, inside the zone and deviating module outside the zone, E_0, Fig. 11.

The FE-results are plotted in Fig. 12a as the circles. Especially for $r/\omega < 0.3$ the displacements for small Young's modules are strongly increased. For $r/\omega > 1$ the further increase of COD is the same independent on the module E and the curves all appear to be parallel. The near-tip behaviour leads the observer to believe that "crack-tip blunting" would occur.

The reciprocal near-tip displacements $1/\delta$ obtained for $r/\omega \to 0$ are plotted in Fig. 12b (circles) versus $\sqrt{E}$. The results deviate from the straight line representing eq.(18). However the general trend, given by eq.(18) is confirmed at least roughly.

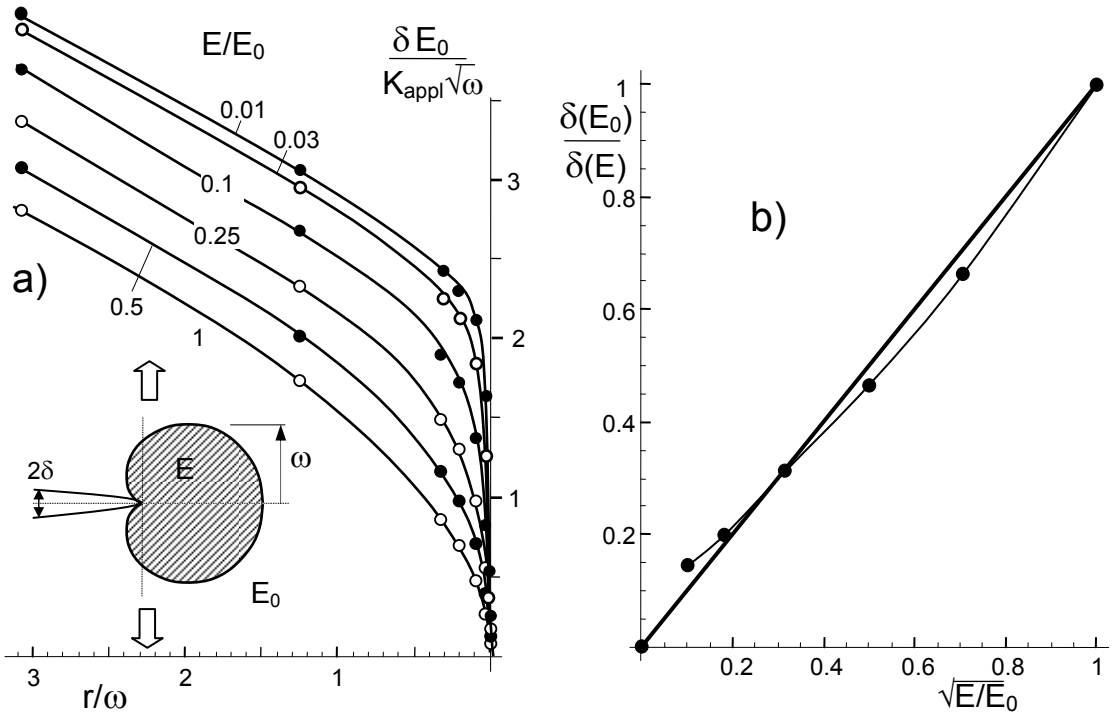

Fig. 12 a) Normalized near-tip displacements for heart-shaped zones with different Young's modulus; b) displacements under constant externally applied stress intensity factor, K_{appl}, as a function of Young's modulus: Symbols for heart-shaped zones, straight line for the crack tip inside the zone.

B) PORES

In order to allow application of continuum mechanics relations in terms of stresses and strains, the complicated SiO_2 micro structure is simplified as shown in Fig. 13. Figure 13a shows a volume element of the silica network containing rings of different size. The largest are indicated by the dashed circles. Figure 13 illustrates the simplification by spherical pores.
For all computations the Poisson's ratio ν=0.17 was used.

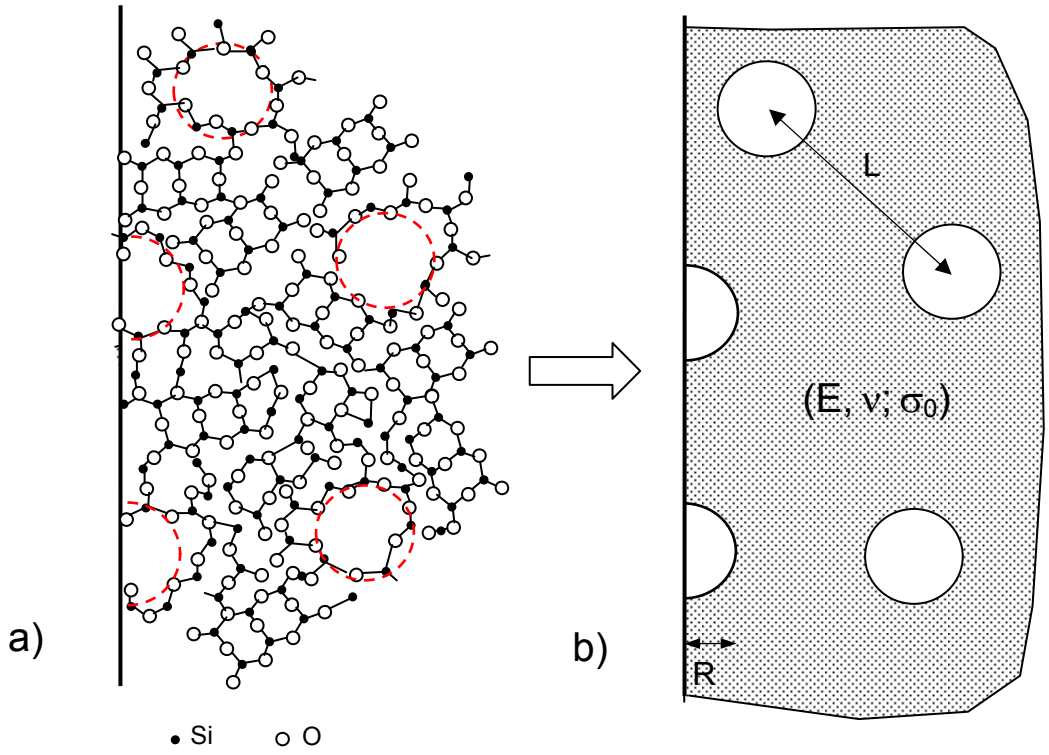

Fig. 13 a) Silica network, b) large SiO_2 rings replaced by nano-pores.

6. 2-dimensional array of half-spherical surface pores

Figure 14a shows a symmetry element of a two-dimensional array of semi-spherical pores at a flat surface. The radius of the half-sphere is R and the distance to the next one $2H$. The applied stress is denoted as σ_∞. The stresses σ_y along the equator between points (A) and (B) are represented in Fig. 14b for several values of H/R. Figure 14c shows the reciprocal stress at the surface and the deepest point as a function of R/H.
The stresses σ_y at the surface points, (B), and the deepest point (A) can be approximated for $R/H<0.8$ by

$$\left.\frac{\sigma_y}{\sigma_\infty}\right|_{(B)} = \frac{1}{0.51 - 0.254\left(\frac{R}{H}\right)^2 - 0.255\left(\frac{R}{H}\right)^4} \qquad (19)$$

$$\left.\frac{\sigma_y}{\sigma_\infty}\right|_{(A)} = \frac{1}{0.503 - 0.197\left(\frac{R}{H}\right)^2} \tag{20}$$

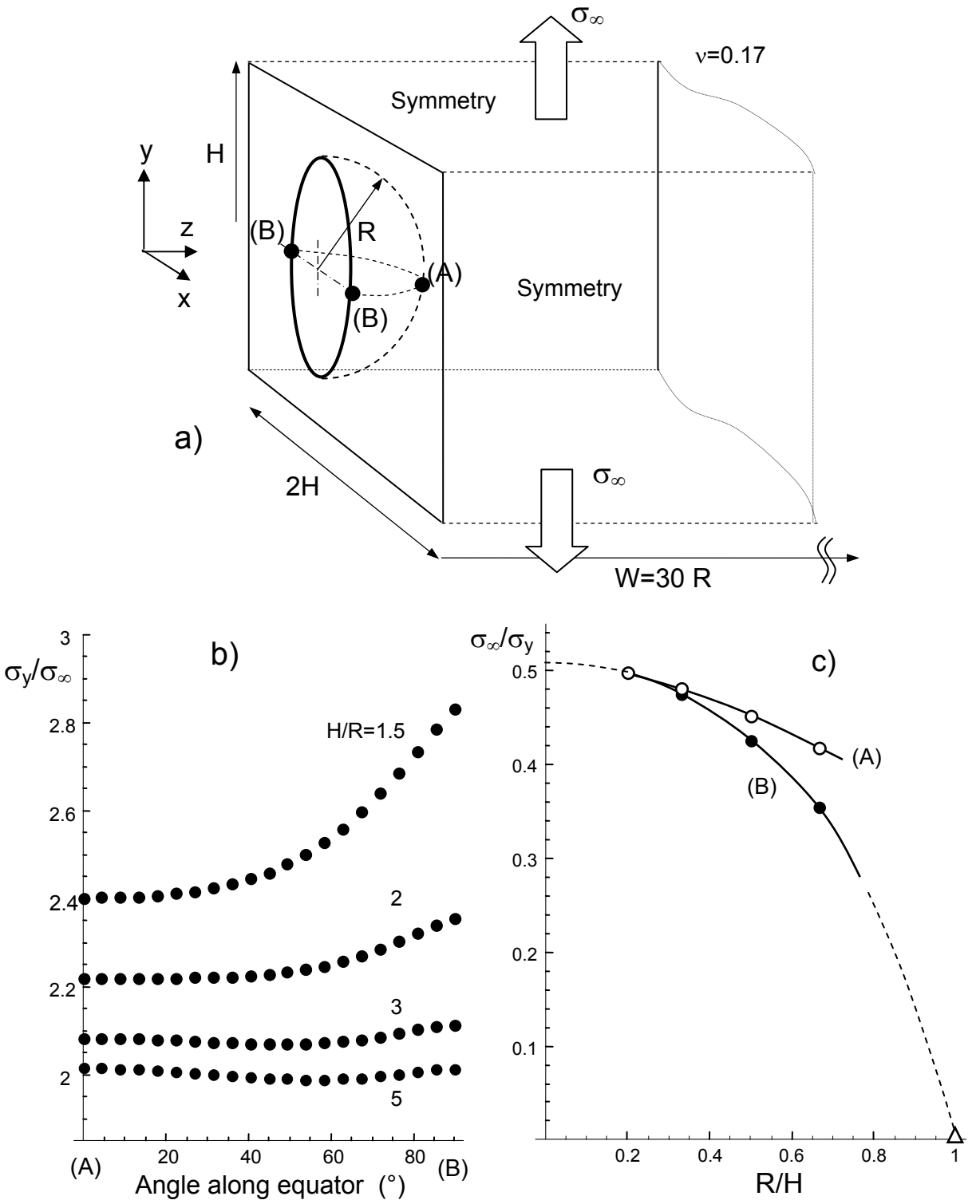

Fig. 14 a) Semi-spherical surface pore, b) stress distribution σ_y along the equator, c) reciprocal stresses, $1/\sigma_y$ at the surface (B) and the deepest point (A), ν=0.17.

7. Description of broken bonds by a circular internal notch

In the preceding considerations, it was assumed that no interaction of the bond-breaking events is present. For very high stresses, this cannot be guaranteed.

On one hand side, a stress concentration occurs around a broken bond since the surrounding bonds must transfer the load that was originally carried by this bond. The increased load in the neighboured bonds causes an increased failure probability by stress-enhanced hydroxyl generation.

On the other side, also the displacements between the original bond partners are increased. Consequently, the reverse reaction in (1) may be hindered somewhat resulting in an increased hydroxyl concentration.

A SiO_2-ring of the silica network may be described by a spherical (nano)-void in a continuous material. This allows a fracture mechanics treatment by an FE-study. According to the finite crack-tip curvature for cracks, the radius of such a void has to be expected in the order of $\rho = 0.5$ nm [12], Fig. 15. Under a load in z-direction, the red Si-O-bond may be cracked by reaction with molecular water (blue/red). Since the open bond cannot transfer load, the void now acts as a disk-like defect of length $2(\rho+L)$ oriented perpendicular to the load direction.

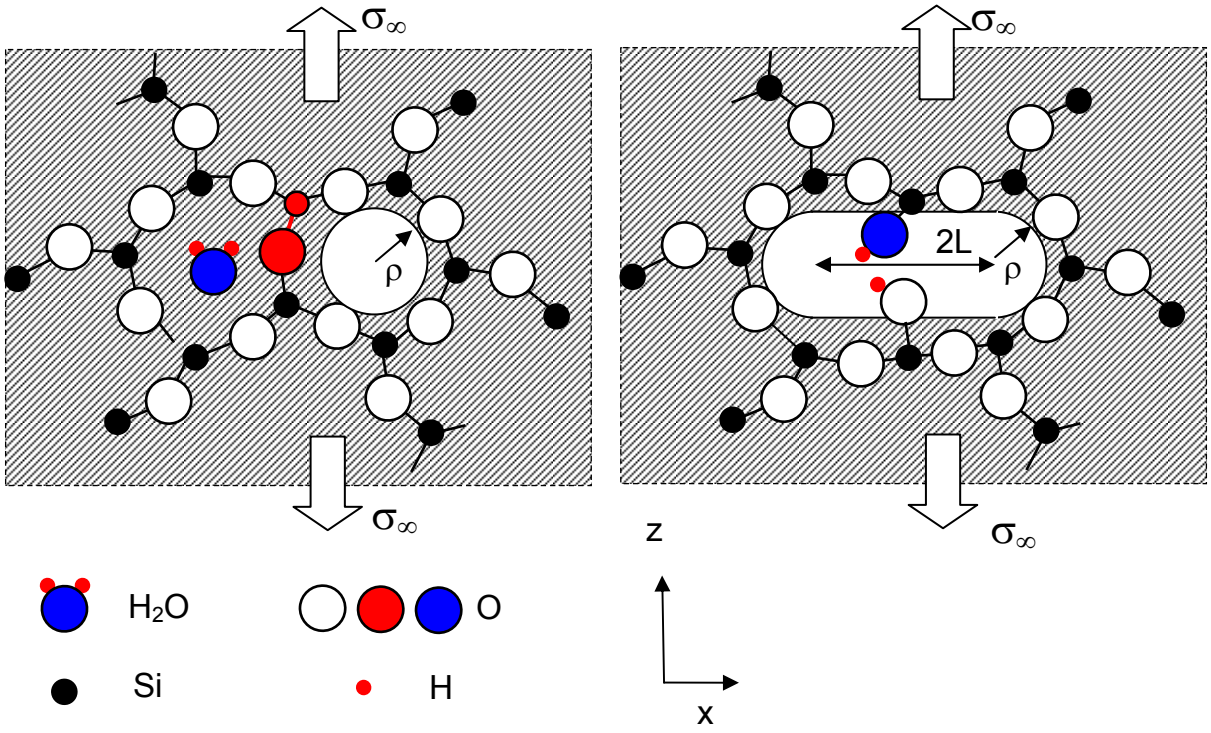

Fig. 15 Left: Bond breaking under uni-axial tension by reaction with molecular water (attacked SiO-bond in red); right: open bond represented by a disk-like notch of diameter $2(\rho+L)$.

The stress increase $\sigma_{max}/\sigma_\infty$ at the notch root is shown in Fig. 16a as a function of the length L (circles). A rough representation of these data may be given by the simple relation

$$\frac{\sigma_z}{\sigma_\infty} = 1.48 + \sqrt{1.84 + \frac{L}{\rho}} \tag{21}$$

The maximum displacement in the centre is given in Fig. 16b. The straight-line dependency is represented by

$$\delta_z \frac{E}{\rho \sigma_\infty} = 2 + 1.275 \frac{L}{\rho} \tag{22}$$

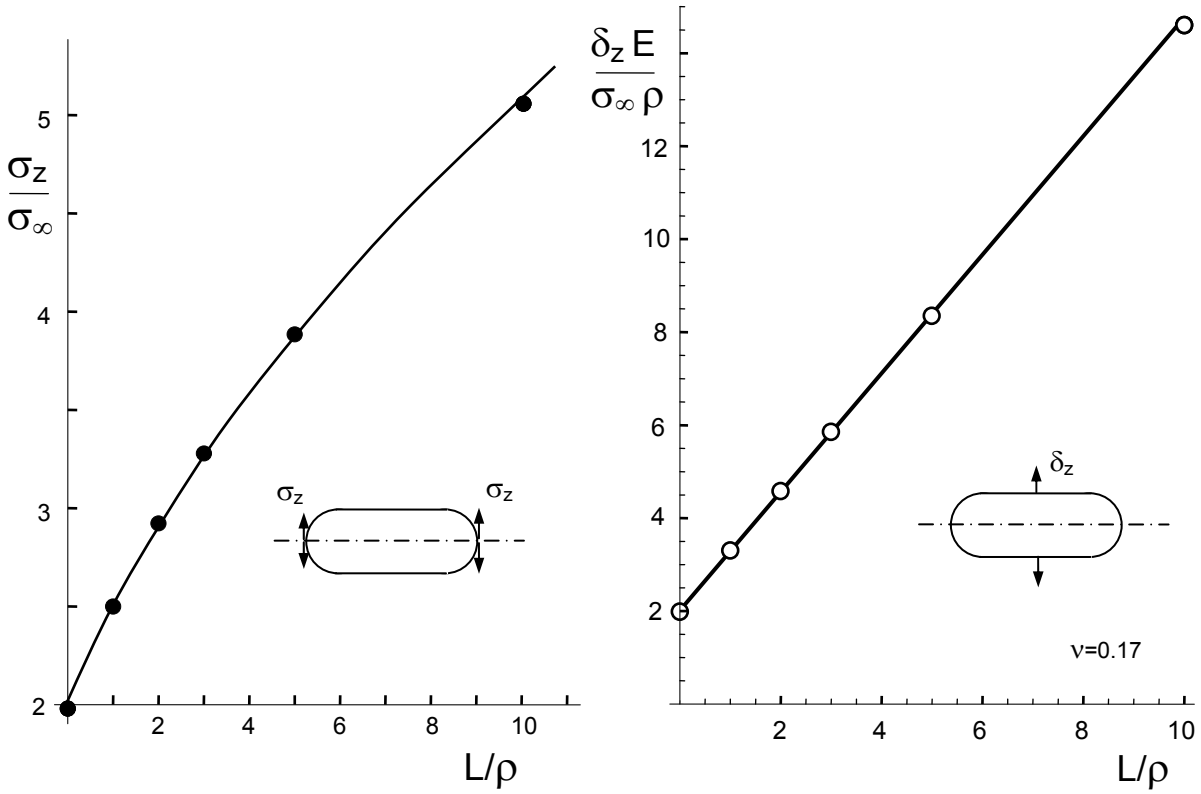

Fig. 16 a) Stress concentration at the notch root for several values of notch length *L* (circles: FE-results, curve: approximation by eq.(21), b) displacements in the axis direction.

References

1 Doremus, R.H., Diffusion of water in silica glass, J. Mater. Res. **10**(1995), 2379-89.

2 R.M. McMeeking, and A.G. Evans, "Mechanics of Transformation-Toughening in Brittle Materials," *J. Am. Ceram. Soc.* **65** 242-246 (1982).

3 S.M. Wiederhorn, T. Fett, G. Rizzi, M.J. Hoffmann and J.P. Guin, "The effect of water penetration on crack growth in silica glass," *Engng Fract Mech,* (2012).

4 O.L. Bowie, Solutions of plane crack problems by mapping technique, in: Mechanics of Fracture (Ed. S.C. Sih), Vol. 1, (1973), 1-5, Noordhoff International Publishing, Leyden.

5 Fett, T., Munz, D., Stress intensity factors and weight functions, Computational Mechanics Publications, Southampton, 1997.

6 M. Isida and H. Tsuru, *Transactions Japan Society of Mechanical Engineers* **49** (1983) 641-645.

7 McMeeking, R.M., Evans, A.G., Mechanics of Transformation-Toughening in Brittle Materials, J. Am. Ceram. Soc. **65**(1982), 242-246.

8 Budiansky, B., Hutchinson, J.W., Lambropoulos, J.C., Continuum theory of dilatant transformation toughening in ceramics, Int. J. Solids and Structures, **25**(1989), 635-646.

9 Fett, T., Guin, J.P., Wiederhorn, S.M., Interpretation of effects at the static fatigue limit of soda-lime-silicate glass, Engng. Fract. Mech. **72**(2005), 2774-279**.**

10 D.M. Stump and B. Budiansky, Crack-growth resistance in transformation-toughened ceramics. *Int. J. Solids Structures* **25**(1989), 635-46.

11 T. Fett, Application of the weight function and boundary collocation method to the calculation of initial phase transformation zones, Engng. Fract. Mech. **52**(1995), 853-863.

12 S.M. Wiederhorn, E.R. Fuller, Jr. and R. Thomson, "Micromechanisms of crack growth in ceramics and glasses in corrosive environments," Metal Science, **14**(1980), 450-8.

KIT Scientific Working Papers
ISSN 2194-1629

www.kit.edu